Research in Astronomy and Astrophysics, 24:085013 (10pp), 2024 August https://doi.org/10.1088/1674-4527/ad6350

Understanding the Activity Performance of Comets 38P/Stephan-Oterma, 64P/Swift-Gehrels and C/2017 M4 (ATLAS) through Broadband Photometric Observations

Xuan Zhang, Jin-Zhong Liu, and Le-Tian Wang
Xinjiang Astronomical Observatory, Chinese Academy of Sciences, Urumqi 830011, China; liujinzh@xao.ac.cn
Received 2024 February 18; revised 2024 July 6; accepted 2024 July 10; published 2024 August 7

Abstract

In this work, we report observations of three comets: 38P/Stephan-Oterma, 64P/Swift-Gehrels, and C/2017 M4 (ATLAS), conducted with the Nanshan one-meter wide-field telescope in 2018 August and November, and 2019 January. We extracted morphological features through image enhancement techniques and calculated the dust activity parameter, $Af\rho$, along with dust mass loss rates and coma color indices using broadband photometric data. Our morphological analysis uncovered a spectrum of dust characteristics among the observed comets, ranging from a significant twisted structure in comet 38P/Stephan-Oterma's coma to the regular coma envelope surrounding comet 64P/Swift-Gehrels. The $Af\rho$ values varied between 148.8 ± 0.3 cm for 64P/Swift-Gehrels and 1118.5 ± 6.2 cm for C/2017 M4 (ATLAS) (measured within a reference aperture radius of $\rho = 6''$), indicating a range from moderate to high activity levels. Dust mass loss rates were estimated from 328.1 kg s^{-1} for comet 64P/Swift-Gehrels to 1395.5 kg s^{-1} for comet C/2017 M4 (ATLAS). The color indices of comets 38P/Stephan-Oterma and C/2017 M4 (ATLAS) closely resemble the average colors of active short-period comets and active long-period comets, respectively. In contrast, 64P/Swift-Gehrels exhibits a significantly bluer hue than typical Jupiter family comets.

Key words: comets: general – comets: individual (38P/Stephan-Oterma, 64P/Swift-Gehrels, C/2017 M4 (ATLAS)) – techniques: photometric

1. Introduction

The prevalent view is that comets are the remnant of icy planetesimals or building blocks left over from the formation of the solar system. Understanding the physical and chemical properties of these early solar system components is a formidable challenge, essential for unraveling the mysteries of planetary formation and probing fundamental questions, such as the origins of Earth's water (e.g., Alexander et al. 2018). This understanding is drawn from studying comets, particularly their activity manifested through dust/gas comas and characteristic tails, driven by solar heating and water ice sublimation (Whipple 1950).

The primary source of cometary activity is the sublimation of volatile materials such as water ice, carbon oxides, and other organic molecules. This sublimation varies with the comet's heliocentric distance, influencing the dominant volatile materials in the outgassing activity of cometary nuclei, which comprise numerous chemical species. Significantly, within the region extending up to three astronomical units (au) from the Sun, the sublimation process of water ice, the primary volatile constituent, primarily propels comet activity. However, sustaining activity beyond this boundary is challenging due to reduced solar radiation exposure. Instances of water-ice-dominated activity have been documented at distances as distant as 5 au from the Sun (Meech et al. 1986).

Besides water ice, carbon dioxide, the second most prevalent volatile in cometary nuclei, can undergo sublimation at greater heliocentric distances, thereby contributing to coma activity (Feaga et al. 2007; A'Hearn et al. 2011; Wesołowski 2022). The cometary nucleus could also have exhibited seasonal effects influenced by its spin rate and orientation, resulting in regional temperature increases and subsequent outgassing activities. Thus, outgassing is often a result of complex physical and chemical processes, not solely reliant on water sublimation. Recent broadband observations have significantly advanced our understanding of cometary activity (Boehnhardt et al. 2007; Hsieh et al. 2011; Jewitt 2015; Shi et al. 2019; Betzler & de Sousa 2020; Xu et al. 2022). Our study focuses on comets 38P/Stephan-Oterma, 64P/Swift-Gehrels, and C/2017 M4 (ATLAS).

38P/Stephan-Oterma: A short-period comet (SPC), exhibiting an eccentricity of 0.859999 and an inclination to the ecliptic plane of 17°.9818, was identified through observations made with the Pan-STARRS 1 telescope. It lastly reached perihelion on 1980 December 5. This comet ranges from a perihelion of

1.57 au simply outside of the orbit of Mars, to an aphelion of 20.9 au, near the orbit of Uranus. Bair et al. (2022) found that during the 2018/19 period, Comet 38P/Stephan-Oterma reached its peak production rate one month before its perihelion approach. They also noted a substantial disparity in the abundance of individual gas species, with levels being 1.5–3.0 times higher pre-perihelion than post-perihelion. Moreover, they observed a persistent decline in the comet's production rate over the long term, with a decrease of 1.5–2.5 times recorded during 2018/19. Our observations occurred when it was 1.58–1.74 au from the Sun on its outbound trajectory.

64P/Swift-Gehrels: Discovered in 1889 and subsequently lost until fortuitously recovered by Tom Gehrels in 1973, this comet experienced a favorable apparition in 1981, reaching 11th magnitude. Observation on 1992 February 5, using the Danish telescope at La Silla, revealed a star-like appearance, with no detectable activity observed through profile analysis. Comet 64P/Swift-Gehrels is a Jupiter family comet (JFC) with Tisserand parameters $2 < T_J < 3$ and orbital periods $P < 200$ yr. During the 2018–2019 apparition, numerous outbursts of this comet were documented through observations (Kelley et al. 2019; Xu et al. 2022). The latest outburst occurred around 2019 January 3, as reported by Xu et al. (2022), indicating a mini-outburst with a magnitude of −0.5. During this event, the morphological features of the dust jet became notably prominent in the processed images. It is speculated that both volatile-driven pressure mechanisms and non-volatile-driven pressure mechanisms could have been pivotal in instigating this outburst.

C/2017 M4 (ATLAS): Initially detected with a magnitude of 18.3 by the Asteroid Terrestrial-impact Last Alert System (ATLAS) Team on 2017 June 21, this dynamically new comet presents distinctive features. Orbital analyses categorized it within the dynamically new class of comets based on its original reciprocal semimajor axis ($1/a_0$) of 31×10^{-6} au^{-1} (Mazzotta Epifani et al. 2014; Sárneczky et al. 2016). Such comets represent an early phase of inward migration, hence their designation as "new" comets. They inhabit regions distant from the Sun, spending the majority (>99.9%) of their existence beyond the heliosphere. Consequently, these comets experience minimal solar irradiation and are subject to limited alteration by the solar wind.

Section 2 furnishes comprehensive descriptions of the observational methodologies and the procedures utilized for data reduction pertaining to the cometary observations. Section 3 elucidates the outcomes and ensuing discussions regarding the morphological characteristics, $Af\rho$ parameter, dust mass production rates, and coma color analysis. Finally, Section 4 encapsulates a concise summary of the study's key findings and implications.

2. Observations and Data Reduction

The Nanshan one-meter wide-field telescope (NOWT) (IAU code N87), managed by the Xinjiang Astronomical Observatory, was employed for the observations. The NOWT is outfitted with a conventional Johnson-Cousin-Bessel multicolor filter system, comprising U, B, V, R, and I filters, and an E2V CCD203-82 (blue). The CCD camera features a resolution of 4096×4136 pixels, providing a field of view spanning $1\overset{\circ}{.}3 \times 1\overset{\circ}{.}3$ (Liu et al. 2014). The telescope was configured to accurately track the velocity of the comet during the exposure period. Table 1 provides a concise overview of the observational parameters.

Our photometric analysis was conducted within the Image Reduction and Analysis Facility (IRAF) system. The standard data reduction pipeline commenced with bias subtraction and flat-field correction applied to all images. Bias values were computed by averaging multiple zero-exposure frames, and flat-field corrections were performed using twilight sky images. To improve the photometric accuracy for the comet, a region distant from the nucleus was chosen for background sky statistics using IRAF's PHOT package, followed by aperture photometry on all CCD images (Zhang et al. 2019). The median full-width half maximum (FWHM) of the comet profile in BVR filters, used as the aperture radius for each observational session, was chosen to mitigate magnitude changes due to seeing variations, following the approach of Licandro et al. (2000). As reported by Betzler et al. (2008), the utilization of the coma's FWHM as the photometric aperture mitigates brightness variations caused by changes in atmospheric transparency. The median FWHM of the target comets is 6″, nearly three times larger than the median FWHM of the unsaturated stars in the image. Additionally, the conventional aperture of $\rho = 10{,}000$ km is also employed to derive the comet magnitude. The photometric results for all filters are presented in Table 2.

Absolute photometric calibration was achieved by observing standard stars from Clem & Landolt (2016) during photometric nights. The observations provided crucial parameters, which were then utilized to perform absolute flux calibration (Bai et al. 2020). The magnitude and color errors calculated for each comet primarily comprise the Poisson statistical error of the detected electrons/photons, the constant noise at the sky level, the readout noise of the CCD chip, and errors in atmospheric extinction, zero-point, and color terms in the fitting transformation equation.

3. Results and Discussion

3.1. Coma Morphology

Morphological analysis was crucial for detecting comet dust structures in images (Farnham 2009). To identify different features, filtering techniques were often necessary. Various

Table 1
The Log of the Photometric Observations for the Comets

Comet	Date	r_h (au)	Δ (au)	α (°)	Filter $\times N \times T_{\rm exp}$ (s)	Pixel Size (km px^{-1})
38P/Stephan-Oterma	2018-11-10	1.589	0.873	33.8	$B \times 5 \times 250$, $V \times 5 \times 200$, $R \times 5 \times 180$	712.3
	2019-01-06	1.740	0.806	14.9	$B \times 3 \times 180$, $V \times 3 \times 170$, $R \times 3 \times 170$	657.6
64P/Swift-Gehrels	2018-11-10	1.396	0.457	22.7	$B \times 3 \times 250$, $V \times 3 \times 200$, $R \times 3 \times 200$	372.9
	2018-11-11	1.396	0.458	22.8	$B \times 4 \times 250$, $V \times 4 \times 200$, $R \times 4 \times 180$	373.7
C/2017 M4 (ATLAS)	2018-08-04	3.614	3.283	16.0	$B \times 4 \times 120$, $V \times 4 \times 120$, $R \times 4 \times 120$	2678.7
	2018-08-06	3.606	3.294	16.1	$B \times 5 \times 180$, $V \times 5 \times 180$, $R \times 5 \times 180$	2687.7

Note. r_h represents the heliocentric distance measured in astronomical units; Δ represents the geocentric distance also measured in astronomical units; α denotes the solar phase angle expressed in degrees; and $T_{\rm exp}$ stands for the total exposure time measured in seconds.

Table 2
Photometry, $Af\rho$, Colors and Dust Production Rates of the Comets

Comet	Date	ρ (arcsec)	B (mag)	V (mag)	R (mag)	$B-V$ (mag)	$V-R$ (mag)	$Af\rho$ (cm)	$Q_{\rm dust}$ (kg s^{-1})
38P	20181110	6.0	14.368 ± 0.002	13.451 ± 0.001	13.073 ± 0.002	0.917 ± 0.002	0.378 ± 0.002	369.3 ± 0.7	753.4
		14.0	13.420 ± 0.002	12.537 ± 0.001	12.229 ± 0.002	0.883 ± 0.002	0.308 ± 0.002	344.3 ± 0.6	702.4
	20190106	6.0	14.526 ± 0.002	13.718 ± 0.001	13.210 ± 0.002	0.808 ± 0.002	0.508 ± 0.002	360.3 ± 0.7	696.0
		15.2	13.592 ± 0.002	12.781 ± 0.001	12.184 ± 0.002	0.811 ± 0.002	0.597 ± 0.002	365.7 ± 0.7	706.5
64P	20181110	6.0	14.166 ± 0.002	13.407 ± 0.001	13.050 ± 0.002	0.759 ± 0.002	0.357 ± 0.002	152.4 ± 0.3	336.0
		26.8	13.129 ± 0.002	12.389 ± 0.001	12.187 ± 0.002	0.74 ± 0.002	0.202 ± 0.002	75.3 ± 0.1	166.0
	20181111	6.0	14.123 ± 0.002	13.377 ± 0.001	13.078 ± 0.002	0.746 ± 0.002	0.299 ± 0.002	148.8 ± 0.3	328.1
		26.8	13.086 ± 0.002	12.362 ± 0.001	12.163 ± 0.002	0.724 ± 0.002	0.199 ± 0.002	77.2 ± 0.1	170.2
C/2017 M4	20180804	6.0	16.488 ± 0.009	15.698 ± 0.005	15.208 ± 0.009	0.790 ± 0.008	0.490 ± 0.007	1005.3 ± 8.3	1252.6
		3.7	16.988 ± 0.012	16.215 ± 0.006	15.749 ± 0.011	0.773 ± 0.010	0.466 ± 0.009	982.5 ± 10.0	1224.2
	20180806	6.0	16.317 ± 0.007	15.708 ± 0.003	15.091 ± 0.006	0.609 ± 0.006	0.617 ± 0.005	1118.5 ± 6.2	1395.9
		3.7	16.868 ± 0.009	16.281 ± 0.005	15.676 ± 0.009	0.587 ± 0.007	0.605 ± 0.007	1049.7 ± 8.7	1309.6

Note. $Af\rho$ is obtained from the aperture of ρ in the R band; The magnitude error is determined by the combined effects of the photometric error and the calibration error associated with the standard stars.

image processing techniques have been meticulously applied to broadband comet images in numerous prior studies (Larson & Slaughter 1992; Schleicher & Farnham 2004; Samarasinha et al. 2006; Lin et al. 2013; Shi et al. 2023). In our work, two image enhancement methods were employed.

The initial method, termed azimuthal renormalization, involves adjusting the brightness at each pixel by normalizing it with the mean value of a surrounding ring centered on the comet's nucleus. This approach enhances contrast and aids in identifying structural features, thereby mitigating the overall brightness gradient originating from the nucleus (Samarasinha & Larson 2014). The second technique, pioneered by Sekanina & Larson (1984) (S&L), involves subtracting a rotated version of the image from the original to derive a rotational derivative. This method excels in identifying structures that radiate outward from the nucleus, especially those resulting from the collective movement of particles drifting away in tandem with the nucleus' rotation. To reduce the influence of the gas emission line as much as possible, the R-band was used to find out the distinct dust features in our images. Figures 1(a)–(c) show the well-developed comas and tails of the three comets. The features processed by these methods are in Figures 2–4. While various feature enhancement techniques aim to minimize errors, factors such as image signal-to-noise ratio, spatial resolution, observation geometry, and proximity to Earth can influence the extraction of coma features. Extracting useful information from these faint features remains challenging.

For comet 38P/Stephan-Oterma, the coma structure can be clearly distinguished in the R-band images by two image-enhanced methods. On 2018 November 10, the radial-normalized image vividly highlights the existence of a sweeping twisted formation, predominantly extending toward the southern direction. The same situation was noticed on 2019 January 6. The overall appearance of the coma may be explained by radiation pressure bending a fan in the direction of the tail, but it may also be an indication of nucleus rotation caused by an active region on the comet's nucleus. The special structures in the dust coma of 38P/Stephan-Oterma were highlighted in the image that was improved using the S&L

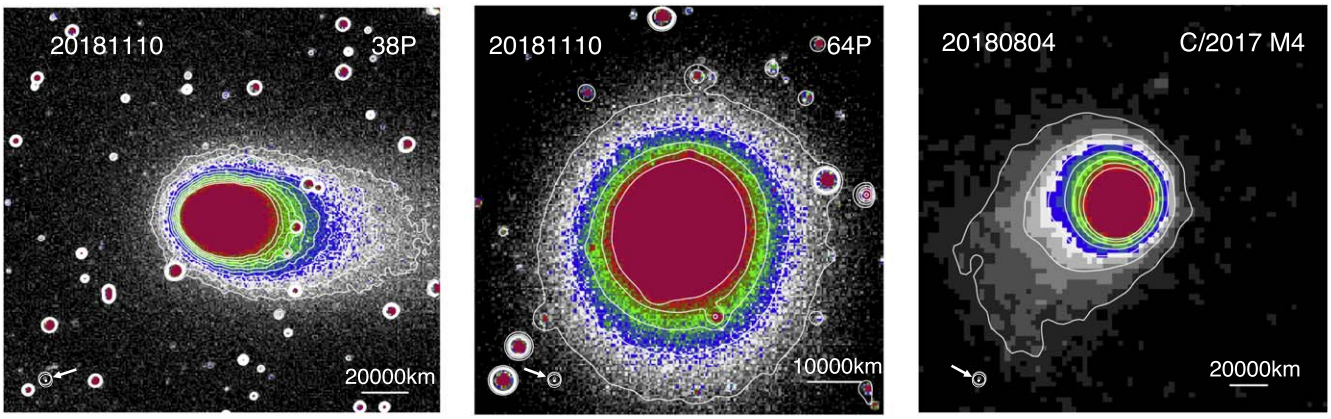

(a) (b) (c)

Figure 1. (a) Isophote of the original image of comet 38P/Stephan-Oterma taken on 2018 November 10; (b) Isophote of the original image of comet 64P/Swift-Gehrels taken on 2018 November 10; (c) Isophote of the original image of comet C/2017 M4 (ATLAS) taken on 2018 August 4.

filtering technique. On 2018 November 10, a jet was observed in the anti-tail direction. On 2019 January 6, there was a tiny shift in the jet's position in the image.

Comet 64P/Swift-Gehrels is distinguished by a tail that is fan-shaped and stretches southward. This comet exemplifies a typical coma envelope, displaying minimal discernible radial or azimuthal structure within the dust coma. Sekanina (1987) proposed a model of comet morphology based on anisotropic emission. According to this model, the release of gas and dust from discrete active regions in the comet's nucleus induces spatial changes in the coma's structure. If these active regions exist at high latitudes in the comet's nucleus, the ejecta from these regions would sweep out a cone around the comet's axis of rotation. Once the rotation rate falls below the ejection rate, the spiral arms resulting from the rotation merge and fill the cone walls, forming fan-shaped features. Additionally, Xu et al. (2022) identified a similar coma structure in the data from 2019 January, albeit with the fan-shaped structure undergoing dispersion, consolidation, and dispersion again within a few days.

In the case of comet C/2017 M4 (ATLAS), we observed a diffuse twisting structure reminiscent of arcs and/or spirals, albeit scarcely discernible against the overall morphology of the surrounding coma. Modeling suggests that when the comet's rotation axis deviates more than 50° from the observer's line of sight, the emitted jet from its active nucleus region appears as a straight feature. Conversely, as this deviation decreases, the jet's curvature is projected onto the plane of the sky, giving rise to a distinctive spiral arm (Farnham 2009). Jewitt (1997) suggested that the observation of spiral arms in Comet Hale–Bopp during perihelion implies an alignment of the nucleus nearly parallel to its rotation axis at that time. Warell et al. (1999) also observed a similar coma structure in comet C/1995 O1 (Hale–Bopp) from 1997 April 24 to 25.

3.2. Afρ

The $Af\rho$ parameter, commonly employed to characterize comet dust activity (A'Hearn et al. 1984), integrates key factors including the grain albedo (A), the filling factor (f) of the grains in the field of view, and the projected radius (ρ). The $Af\rho$ value is derived from

$$Af\rho = \frac{4 \times r^2 \times \Delta^2 \times 10^{0.4(m_{\rm sun} - m_c)}}{\rho} \quad (1)$$

where r and Δ represent the heliocentric and geocentric distances, respectively. The symbols $m_{\rm Sun}$ and m_c correspondingly denote the apparent magnitude of the Sun in the R-band and the magnitude of the comet measured with an aperture radius of ρ. Table 2 illustrates the respective $Af\rho$ values for each comet, computed utilizing the R-band within a circular aperture of $\rho = 6''$. Analysis reveals that dynamically new comets tend to exhibit higher $Af\rho$ values compared to other comets.

We additionally derived the $Af\rho$ profiles, from which comet behavior may be studied for the best available analysis. Figure 5 illustrates the variation of $Af\rho$ in the R-band as a function of the distance from the nucleus for the target comets. In comet C/2017 M4 (ATLAS), a noticeable reduction in $Af\rho$ correlated with nucleocentric distance ρ. This decline is often attributed to non-steady state dust emission and potential degradation or destruction of dust grains (Tozzi et al. 2003; Lara et al. 2004). Our data did not reveal this drop for comets 38P/Stephan-Oterma and 64P/Swift-Gehrels; this might be due to their small apparent coma expansion and very low activity level. For the three comets analyzed in this research,

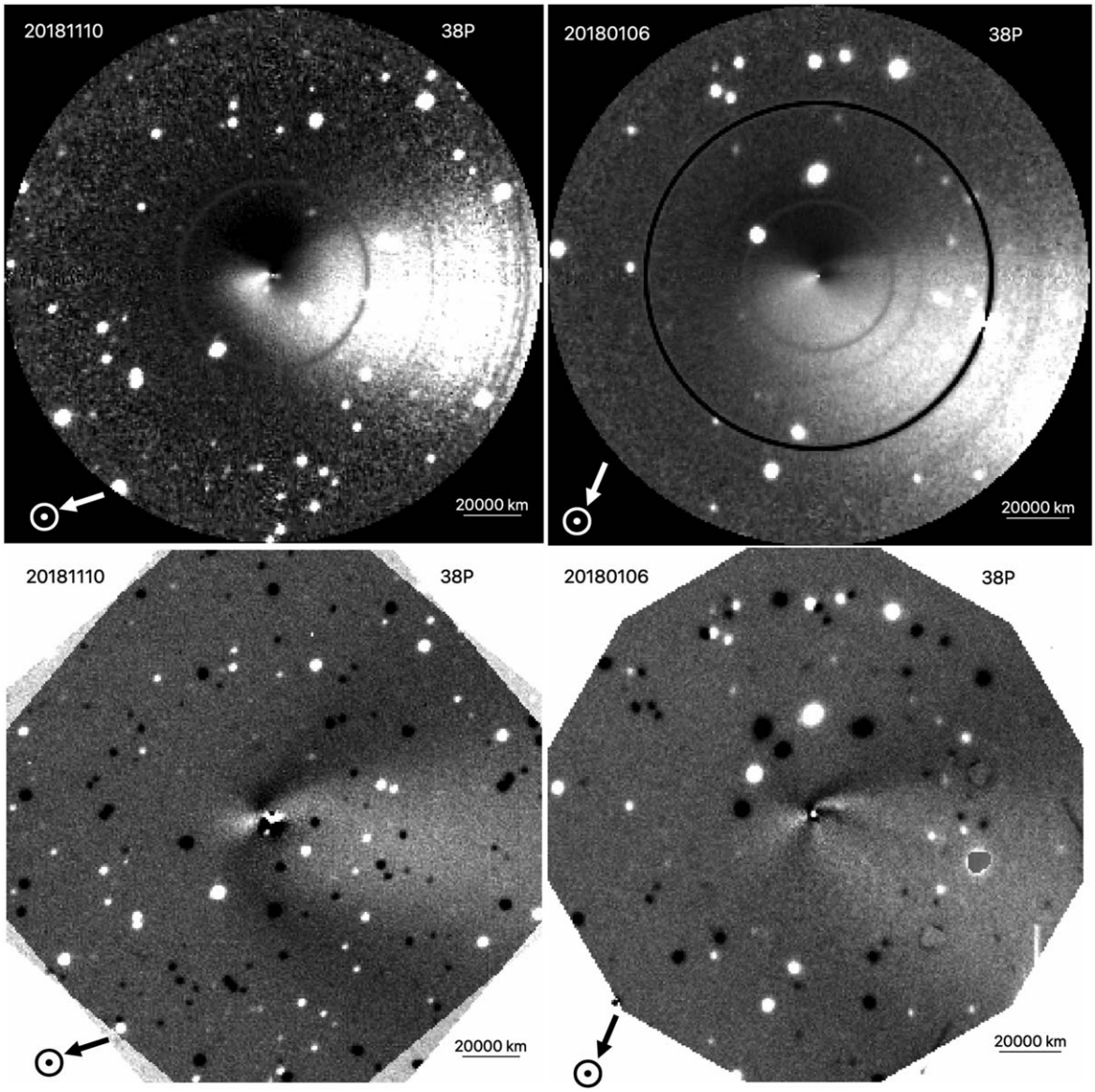

Figure 2. Azimuthal renormalization (top) and S&L (bottom) images obtained in the *R* band for comet 38P/Stephan-Oterma. For the enhancement images, North is up and East is on the left.

the maximum $Af\rho$ reached at low ρ; however, comet C/2017 M4 (ATLAS) then exhibits a rather quick decline. The cometocentric distance of comets 64P/Swift-Gehrels and 38P/Stephan-Oterma lies outside of $\rho = 6''$, and both comets have a steady trend. When $Af\rho$ is almost constant in the multi-aperture measurement, it indicates that the dust environment exhibits steady-state emission. Variations in $Af\rho$ at various ρ suggest the possibility of unsteady dust emission within the coma (Shi et al. 2014). However, high dust activity is generally considered to be indicated by a larger $Af\rho$ value. The data acquired from the targets within our sample validate the moderate to high activity levels exhibited by these comets.

3.3. Dust Mass Production Rate

The $Af\rho$ parameter is frequently employed to characterize dust activity; however, it does not offer a direct measure of the dust production rate, $Q_{\rm dust}$. To derive an estimate of the dust mass-loss rate for the comets, we employed the formalism outlined by Weaver et al. (1999)

$$Q_{\rm dust} = \frac{(0.67) \times a_d \times \rho_d \times v_d}{A}(Af\rho) \quad (2)$$

where $Af\rho$ is measured in meters, a_d signifies the mean radius of dust grains, A represents the geometric albedo of the grains, while ρ_d denotes the grain density, and v_d stands for the velocity

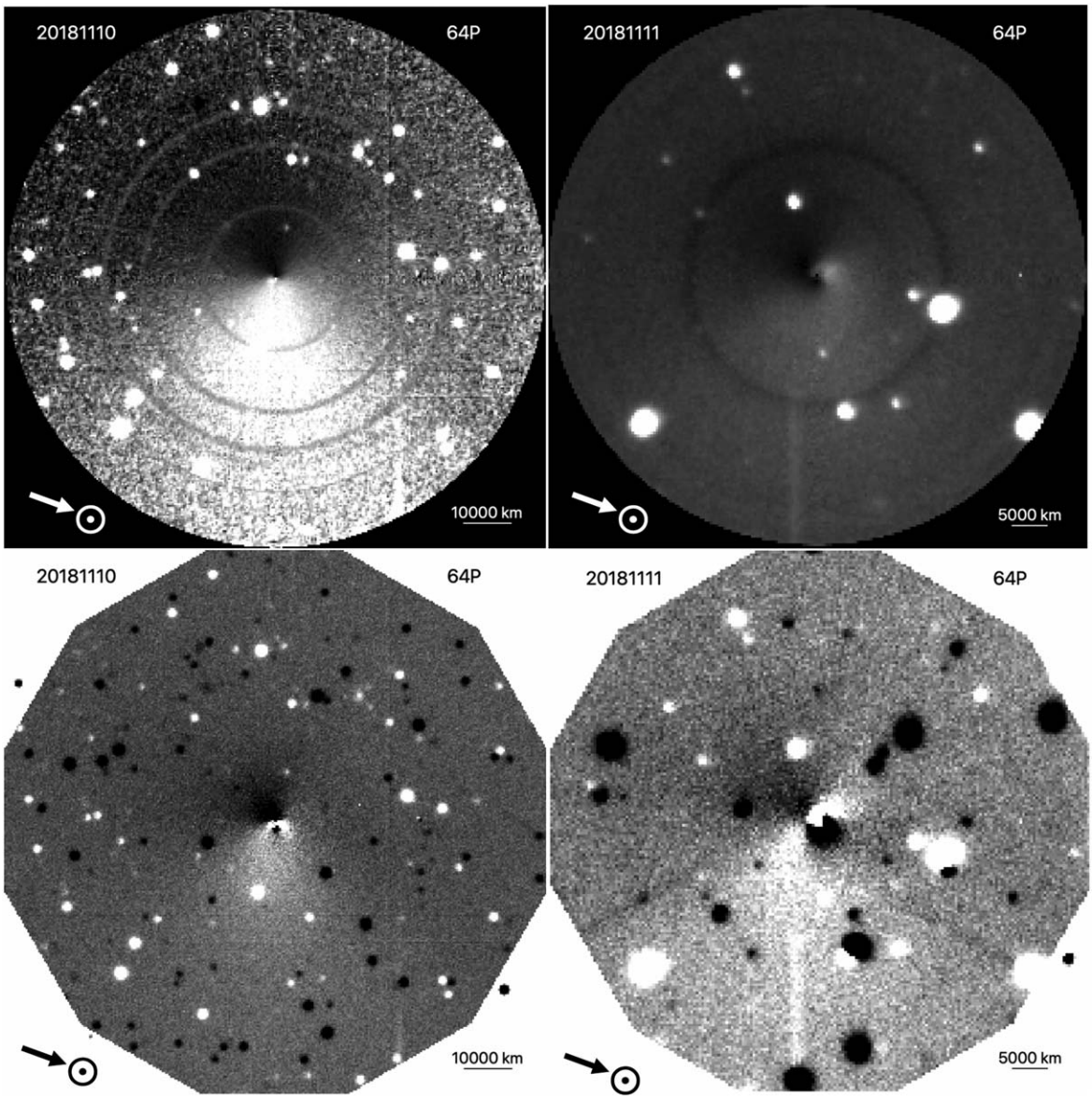

Figure 3. Azimuthal renormalization (top) and S&L (bottom) images obtained in the *R* band for comet 64P/Swift-Gehrels. For the enhancement images, North is up and East is on the left.

of grain ejection. In our analysis, we employed the $Af\rho$ values previously computed for the aperture of $\rho = 6''$. While $Af\rho$ is theoretically impacted by the aperture size, obtaining a quantitative assessment of the dust generation rate heavily relies on the characteristics of the dust environment, necessitating assumptions and estimates regarding particle density, size, and outflow velocity. In this study, we adopted typical values, including an albedo (A) of 0.04, an average grain radius ($\langle a \rangle$) of 30 μm within the coma. Assuming the expansion speed of the dust grains is represented by the empirical relation $v_{\rm dust} = 0.536 \cdot r_h^{-0.6}$ km s^{-1} (Bobrovnikoff 1954; Whipple 1978).

Utilizing Equations (1) and (2), the dust mass production rates of comets were estimated. For comet 38P/Stephan-Oterma, the dust mass-loss rate $Q_{\rm dust}$ was determined to be 753.4 kg s^{-1} on 2018 November 10, and 696.0 kg s^{-1} on 2019 January 6, respectively. Regarding comet 64P/Swift-Gehrels, the $Q_{\rm dust}$ was calculated as 336.0 kg s^{-1} on 2018 November 10, and 328.1 kg s^{-1} on 2018 November 11, respectively. Finally, for comet C/2017 M4 (ATLAS), the $Q_{\rm dust}$ was estimated to be 1252.6 kg s^{-1} on 2018 August 4, and 1395.5 kg s^{-1} on 2018 August 6, respectively.

3.4. Color Index

Spectral analysis offers insights into the chemical composition of celestial bodies within the solar system. However, the

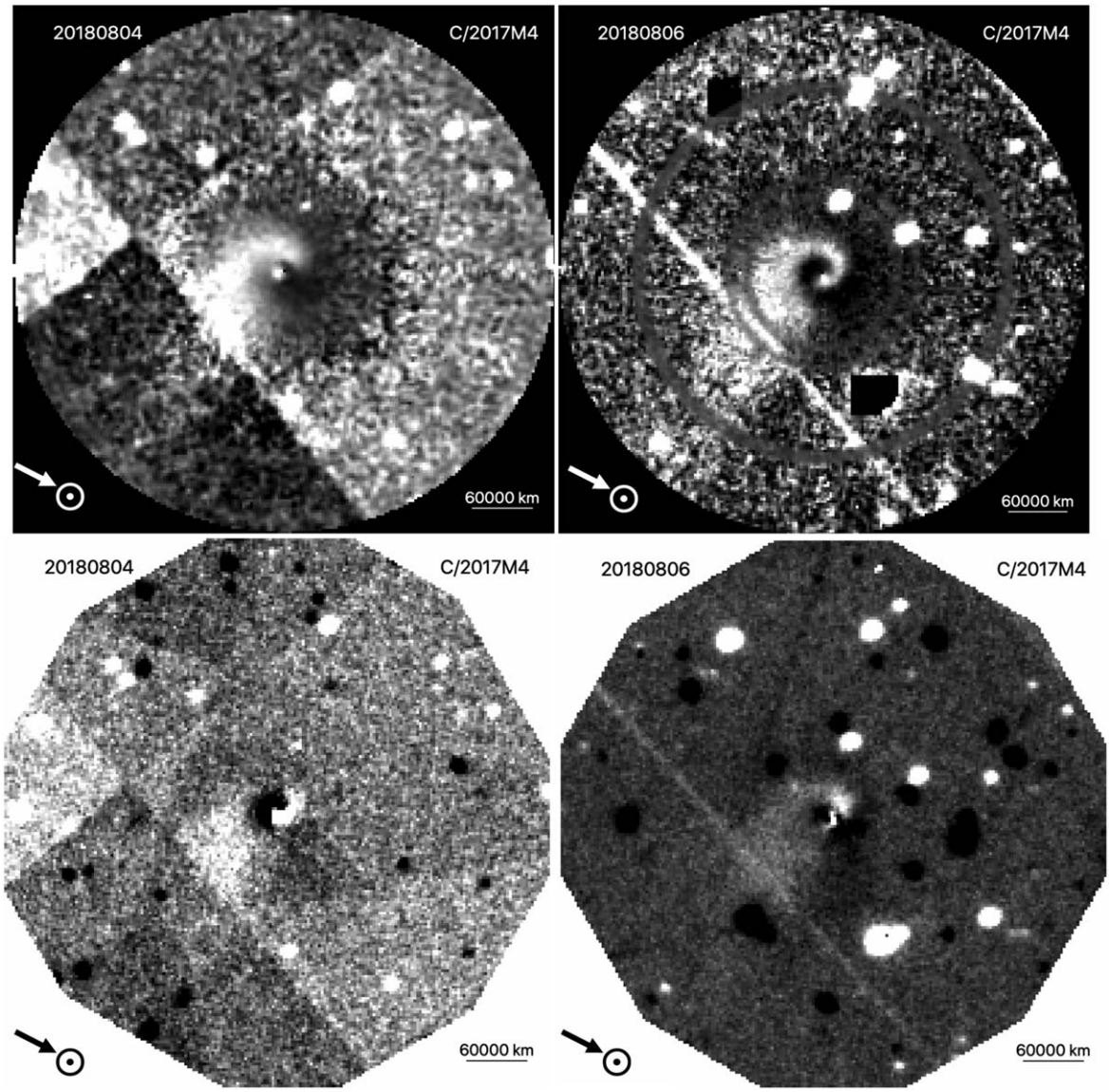

Figure 4. Azimuthal renormalization (top) and S&L (bottom) images obtained in the *R* band for comet C/2017 M4 (ATLAS). For the enhancement images, North is up and East is on the left.

majority of solar system objects are too faint to be observed in terms of their spectra. Instead, we employ broadband colors from filters as a proxy. Even though compositions cannot be uniquely obtained from colors alone, they are useful for comparing different kinds of objects. Investigating alterations in color as one moves away from the center of the coma offers valuable insights into potential fluctuations in the optical characteristics of dust grains within the coma, which could be influenced by phenomena like sublimation or fragmentation (Mazzotta Epifani et al. 2014). Before commencing the analysis, it is crucial to consider the potential influence of gas emission on the signal detected through broad-band filters in comets. The broad spectral range covered by CN to NH_2 lines enables their contribution to the overall flux captured by filters *B* and *V*. Furthermore, due to band overlap, several spectral lines of various chemical species can be detected simultaneously in these filters. Conversely, lines such as NH_2, CN, H_2O+, and C_2, which exhibit lower intensities or are absent in comets, do not notably impact the flux recorded by filters *R* and *I*. Variations in the intensity of these lines and the continuum, linked to nuclear activity, may potentially manifest in the *BVRI* color measurements (Betzler et al. 2017). Some previous spectral and polarization studies have shown that the contribution of gas emission to the total comet flux measured with broadband filters is generally weak (Jewitt et al. 1982; Zubko et al. 2014). Unfortunately, as we do not have any

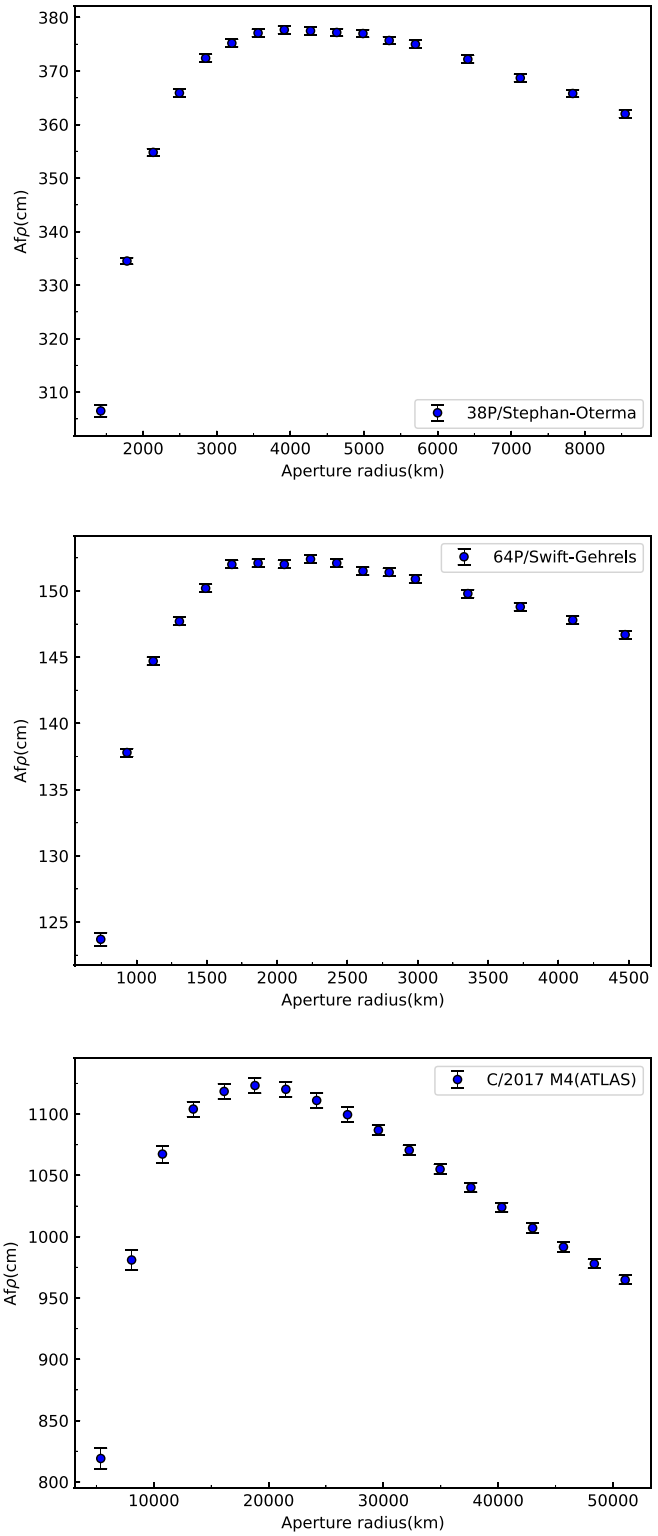

Figure 5. *R*-band $Af\rho$ trend vs. cometocentric distance obtained for target comets. Top: 38P/Stephan-Oterma; middle: 64P/Swift-Gehrels; Bottom: C/2017 M4 (ATLAS).

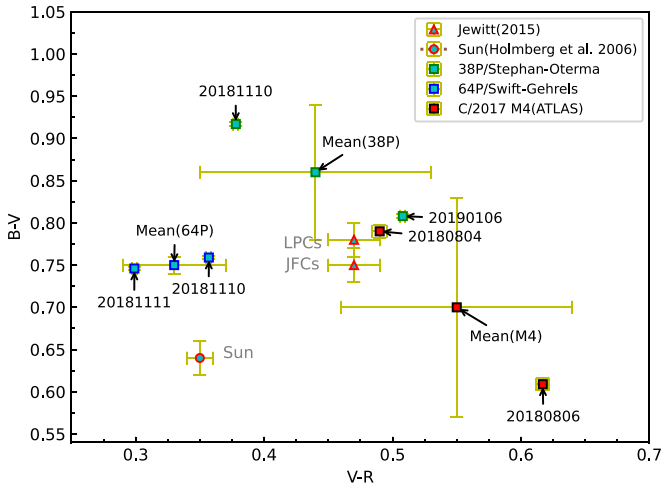

Figure 6. The color–color diagram compares the data from our study (squares) with data from other studies (triangles). The color of the Sun is marked (dot). Error bars represent the 1σ standard deviation of the mean value.

spectroscopic data for the comets, we cannot estimate the gas contamination to dust production. Therefore, Colorimetric data can generally be applied to constrain cometary species' physical and chemical attributes (Ivanova et al. 2017).

The data collected during the observational period facilitated the analysis of the coma colors displayed by the three comets. Table 2 provides a summary of the colors obtained at the optical aperture with a radius of $\rho = 6''$. It is crucial to emphasize that the color index is heavily influenced by observational and data reduction parameters, including the aperture size utilized for magnitude calculations. Additionally, coma colors reflect integrated characteristics, thus strongly influenced by short-term changes in dust spatial distribution. Variations exceeding photometric uncertainty in $B-V$ and $V-R$ colors may stem from differences in observing conditions and intrinsic alterations in coma characteristics, including composition and dust size distribution (Mazzotta Epifani et al. 2011).

Figure 6 displays a broadband color diagram depicting $B-V$ versus $V-R$. The data points (squares) in this study are calculated as the mean of two measurements taken for the same target, as presented in Table 2, while the solar color indices utilized herein are $B-V=0.64\pm0.02$ and $V-R=0.35\pm0.01$ (Holmberg et al. 2006). Additionally, other data points (triangles) are sourced from Jewitt (2015). In contrast, Solontoi et al. (2012) determined the mean colors of SPCs in the Sloan filter system and converted them to *BVR*, revealing $B-V=0.75\pm0.02$ and $V-R=0.46\pm0.02$ (Jewitt 2015). These values are in reasonable concordance with the average color indices observed for comet 38P/Stephan-Oterma. The

$B-V$ value of 64P/Swift-Gehrels is in agreement with the JFCs' mean value. However, the $V-R$ value of 64P/Swift-Gehrels is lower than the mean value, suggesting that it appears bluer than the majority of JFCs.

Between 2018 August and September, approximately two months prior to our observations, the reported color conversion to the *BVRI* system was $V-R=0.30\pm0.02$ (Kelley et al. 2019), which aligns closely with our findings. Subsequent observations by Xu et al. (2022) indicated even bluer colors, suggesting a bluing process occurring in 64P/Swift-Gehrels between 2018 September and November. This phenomenon could potentially signify the release of primitive materials from within the comet's nucleus. A similar bluing effect was observed recently in comet C/2019 Y4 (ATLAS) prior to its fragmentation event, indicating significant gas release. As proposed by Betzler & de Sousa (2020), deviations from the average color of the comet might indicate changes in particle size distribution or composition. Consequently, our data set currently lacks sufficient evidence to establish a definitive explanation for the bluish appearance of comet 64P/Swift-Gehrels.

We note that the two adjacent observations of comet 38P/Stephan-Oterma shown in Figure 6 were made nearly two months apart, and the color of the coma reddened over time. Similar color changes were observed for comet C/1995 O1 (Hale–Bopp) (Weiler et al. 2003) and comet C/2013 A1 (Siding Spring) (Li et al. 2013), despite their different spatial scale distributions. Li et al. (2013) interpreted the spatial color distribution of comet C/2012 S1 (ISON) as indicative of water ice particles in the coma. As these ice particles move away from the nucleus, they slowly sublimate, causing the coma to redden. Weiler et al. (2003) suggested that the color of dust generally depends on the size, shape, and optical constants of the dust particles. Given that the shape and optical constants of cometary dust do not change significantly with variations in heliocentric distance, the size distribution of dust particles is likely the primary factor influencing the observed reddening. Due to the lack of evidence, we cannot determine the specific changes that occurred to comet 38P/Stephan-Oterma during the period between observations.

As depicted in Figure 6, the color indices of comet C/2017 M4 closely resemble the mean color of active long-period comets (LPCs). In our study, the color index $B-V$ of comet C/2017 M4 exhibits significant variations on short timescales. These variations are not attributable to observational changes or data processing errors, and the dust production rate remains relatively stable during this period. Previous research has indicated that phase changes can lead to alterations in the coma's color (Zubko et al. 2014), but this explanation is not applicable to comet C/2017 M4, as the phase angle remains nearly constant throughout the observation period. Additionally, the particle size sorting effect described by Fink & Rubin (2012) cannot account for the observed changes due to the short timescale, which is insufficient for large particles to diffuse into the outer coma. The observed color index variations may be linked to intrinsic activity during the observation period. Ivanova et al. (2017) attributed the unusual color changes in comet C/2013 UQ4 (Catalina) to variations in the heterogeneous nuclear composition using a dust grain model (Ivanova et al. 2016). They also noted the difficulty in determining the dust color index from a single observation.

4. Summary

This study presents observations of comets 38P/Stephan-Oterma, 64P/Swift-Gehrels, and C/2017 M4 (ATLAS) conducted with the NOWT. Our focus was on understanding their activity through morphological methods and photometric analysis. Key findings include:

(i) These comets with a wide range of characteristics were subjected to morphological analysis following the application of enhancing methods to the images. A sizable twisted structure (38P/Stephan-Oterma), morphologies resembling corkscrews (C/2017 M4 (ATLAS)), and wide coma extensions that extended radially away from the nucleus (64P/Swift-Gehrels) were also observed.

(ii) The $Af\rho$ values in the reference aperture of $\rho=6''$ were calculated from the photometry result. The $Af\rho$ values exhibit a wide range, spanning from 148.8 cm for comet 64P/Swift-Gehrels to 1118.5 cm for comet C/2017 M4 (ATLAS), indicating varying degrees of activity among the comets. Notably, the highest and lowest $Af\rho$ values correspond to LPCs and SPCs, respectively. Moreover, utilizing typical parameters in our calculations based on photometric observations, we have derived a quantitative estimate of the dust mass loss rate for the target comet. Results indicated a range from 328.1 kg s^{-1} for comet 64P/Swift-Gehrels to 1395.5 kg s^{-1} for comet C/2017 M4 (ATLAS).

(iii) The average color indices of comet 38P/Stephan-Oterma are in agreement with the mean values of SPCs. Although the 64P/Swift-Gehrels' $B-V$ value agrees with the JFCs' mean value, its $V-R$ value is smaller than the mean value, suggesting a bluer appearance than the majority of the JFCs. The color indices of comet C/2017 M4 (ATLAS) are close to the mean color of active LPCs.

Acknowledgments

We thank the anonymous referee for comments that improved the paper. This research is supported by the Natural Science Foundation of Xinjiang Uygur Autonomous Region of China (grant No. 2021D01B112). We acknowledge the Tianshan Talent Training Program through the grant 2023TSYCCX0101 .

References

A'Hearn, M. F., Belton, M. J. S., Delamere, W. A., et al. 2011, Sci, 332, 1396
A'Hearn, M. F., Schleicher, D. G., Millis, R. L., et al. 1984, AJ, 89, 579
Alexander, C. M. O., McKeegan, K. D., & Altwegg, K. 2018, SSRv, 214, 36
Bai, C.-H., Feng, G.-J., Zhang, X., et al. 2020, RAA, 20, 211
Bair, A., Schleicher, D., Knight, M., et al. 2022, BAAS, 54, 8
Betzler, A. S., Almeida, R. S., Cerqueira, W. J., et al. 2017, AdSpR, 60, 612
Betzler, A. S., & de Sousa, O. F. 2020, NewA, 75, 101320
Betzler, A. S., Ferreira, D. H., Ribeiro dos Santos, T. H., et al. 2008, JALPO, 50, 23
Bobrovnikoff, N. T. 1954, AJ, 59, 356
Boehnhardt, H., Pompei, E., Tozzi, G. P., et al. 2007, A&A, 470, 1175
Clem, J. L., & Landolt, A. U. 2016, AJ, 152, 91
Farnham, T. L. 2009, P&SS, 57, 1192
Feaga, L. M., A'Hearn, M. F., Sunshine, J. M., et al. 2007, Icar, 190, 345
Fink, U., & Rubin, M. 2012, Icar, 221, 721
Holmberg, J., Flynn, C., & Portinari, L. 2006, MNRAS, 367, 449
Hsieh, H. H., Ishiguro, M., Lacerda, P., et al. 2011, AJ, 142, 29
Ivanova, O., Zubko, E., Videen, G., et al. 2017, MNRAS, 469, 2695
Ivanova, O. V., Luk'yanyk, I. V., Kiselev, N. N., et al. 2016, P&SS, 121, 10
Jewitt, D. 1997, EM&P, 79, 35
Jewitt, D. 2015, AJ, 150, 201
Jewitt, D. C., Soifer, B. T., Neugebauer, G., et al. 1982, AJ, 87, 1854
Kelley, M. S. P., Bodewits, D., Ye, Q., et al. 2019, RNAAS, 3, 126
Lara, L.-M., Tozzi, G. P., Boehnhardt, H., et al. 2004, A&A, 422, 717
Larson, S. M., & Slaughter, C. D. 1992, Asteroids, Comets, Meteors 1991 (Houston, TX: Lunar and Planetary Society), 337
Li, J.-Y., Kelley, M. S. P., Knight, M. M., et al. 2013, ApJL, 779, L3
Licandro, J., Serra-Ricart, M., Oscoz, A., et al. 2000, AJ, 119, 3133
Lin, Z.-Y., Lara, L. M., & Ip, W.-H. 2013, AJ, 146, 4
Liu, J., Zhang, Y., Feng, G., & Bai, C. 2014, Setting the Scene for Gaia and LAMOST, Vol. 298 (Tucson, AZ: Univ. Arizona Press), 427
Mazzotta Epifani, E., Dall'Ora, M., Perna, D., et al. 2011, MNRAS, 415, 3097
Mazzotta Epifani, E., Perna, D., Di Fabrizio, L., et al. 2014, A&A, 561, A6
Meech, K. J., Jewitt, D., & Ricker, G. R. 1986, Icar, 66, 561
Samarasinha, N. H., Larson, S., & Beshore, E. 2006, AAS/DPS Meeting Abstracts, 38, 29.13
Samarasinha, N. H., & Larson, S. M. 2014, Icar, 239, 168
Sárneczky, K., Szabó, G. M., Csák, B., et al. 2016, AJ, 152, 220
Schleicher, D. G., & Farnham, T. L. 2004, in Comets II, ed. M. C. Festou, H. U. Keller, & H. A. Weaver (Tucson: University of Arizona Press), 449
Sekanina, Z. 1987, Diversity and Similarity of Comets, 278, 315
Sekanina, Z., & Larson, S. M. 1984, AJ, 89, 1408
Shi, J., Ma, Y., Liang, H., et al. 2019, NatSR, 9, 5492
Shi, J., Xu, R., Ma, Y., et al. 2023, ApJ, 943, 26
Shi, J. C., Ma, Y. H., & Zheng, J. Q. 2014, MNRAS, 441, 739
Solontoi, M., Ivezić, Ž., Jurić, M., et al. 2012, Icar, 218, 571
Tozzi, G. P., Boehnhardt, H., & Lo Curto, G. 2003, A&A, 398, L41
Warell, J., Lagerkvist, C.-I., & Lagerros, J. S. V. 1999, A&AS, 136, 245
Weaver, H. A., Feldman, P. D., A'Hearn, M. F., et al. 1999, Icar, 141, 1
Weiler, M., Rauer, H., Knollenberg, J., et al. 2003, A&A, 403, 313
Wesołowski, M. 2022, RAA, 22, 055015
Whipple, F. L. 1950, ApJ, 111, 375
Whipple, F. L. 1978, M&P, 19, 305
Xu, R. Q., Shi, J. C., Ma, Y. H., et al. 2022, A&A, 665, A79
Zhang, X., Liu, J.-Z., Wang, Y.-H., et al. 2019, RAA, 19, 065
Zubko, E., Muinonen, K., Videen, G., et al. 2014, MNRAS, 440, 2928